ACS APPLIED MATERIALS & INTERFACES

www.acsami.org Research Article

Near-Infrared-Responsive Photo-Driven Nitrogen Fixation Enabled by Oxygen Vacancies and Sulfur Doping in Black $TiO_{2-x}S_y$ Nanoplatelets

Xiaolan Xue,[⊥] Hongwei Chen,[⊥] Yan Xiong, Renpeng Chen, Minghang Jiang, Gao Fu, Zhonghua Xi, Xiao Li Zhang, Jing Ma,* Weihai Fang, and Zhong Jin*

Cite This: *ACS Appl. Mater. Interfaces* 2021, 13, 4975−4983 Read Online

ACCESS | Metrics & More | Article Recommendations | Supporting Information

Downloaded via NANJING UNIV on March 12, 2021 at 08:17:54 (UTC).
See https://pubs.acs.org/sharingguidelines for options on how to legitimately share published articles.

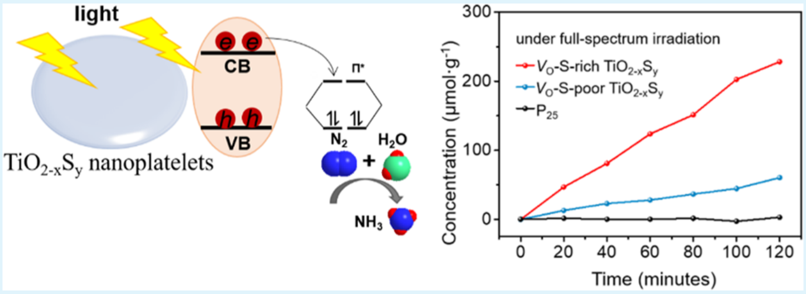

ABSTRACT: Solar-driven nitrogen fixation is a promising clean and mild approach for ammonia synthesis beyond the conventional energy-intensive Haber−Bosch process. However, it is still challenging to design highly active, stable, and low-cost photocatalysts for activating inert N_2 molecules. Herein, we report the synthesis of anatase-phase black $TiO_{2-x}S_y$ nanoplatelets enriched with abundant oxygen vacancies and sulfur anion dopants (V_O-S-rich $TiO_{2-x}S_y$) by ion exchange method at gentle conditions. The V_O-S-rich $TiO_{2-x}S_y$ nanoplatelets display a narrowed bandgap of 1.18 eV and much stronger light absorption that extends to the near-infrared (NIR) region. The co-presence of oxygen vacancies and sulfur dopants facilitates the adsorption of N_2 molecules, promoting the reaction rate of N_2 photofixation. Theoretical calculations reveal the synergistic effect of oxygen vacancies and sulfur dopants on visible−NIR light adsorption and photoexcited carrier transfer/separation. The V_O-S-rich $TiO_{2-x}S_y$ exhibits improved ammonia yield rates of 114.1 μmol g^{-1} h^{-1} under full-spectrum irradiation and 86.2 μmol g^{-1} h^{-1} under visible−NIR irradiation, respectively. Notably, even under only NIR irradiation (800−1100 nm), the V_O-S-rich $TiO_{2-x}S_y$ can still deliver an ammonia yield rate of 14.1 μmol g^{-1} h^{-1}. This study presents the great potential to regulate the activity of photocatalysts by rationally engineering the defect sites and dopant species for room-temperature N_2 reduction.

KEYWORDS: *photocatalytic nitrogen fixation, oxygen vacancies, sulfur doping, black titania, band structure, interfacial engineering*

1. INTRODUCTION

Ammonia is a very important raw material for agriculture and industry. It is also recognized as a promising energy carrier with high mass content of hydrogen (17.6 wt %), good safety, and zero carbon emission.[1−5] The synthesis of ammonia at mild conditions has attracted much attention, but it is still difficult even though nitrogen is abundant in the atmosphere, which shall be ascribed to the extreme stability of the nonpolar N≡N triple bond with a high bond energy of 941 KJ mol^{-1}.[6,7] The primary method for ammonia synthesis in industry is the Haber−Bosch process, which is carried out under harsh temperature (300−500 °C) and high pressure (20−30 MPa).[8,9] It also requires a substantial energy input and emits a large number of greenhouse gases.[10,11] These shortcomings have sparked much interest in developing sustainable and eco-friendly approaches for ammonia synthesis.

Photosynthesis of ammonia from N_2 is emerging as a promising technology for nitrogen fixation at mild conditions.[12,13] Since the ultraviolet light-induced N_2 reduction on TiO_2 was first reported by Schrauzer and Guth in 1977,[14] tremendous efforts have been devoted to improving the photocatalytic performance of TiO_2-based semiconductors.[15−19] However, the photocatalytic activity of TiO_2 is restricted by its poor absorption ability in visible−near-infrared (NIR) region owing to its wide bandgap (3.0−3.2 eV) and low quantum efficiency due to the rapid recombination of photo-

Received: October 6, 2020
Accepted: January 6, 2021
Published: January 19, 2021

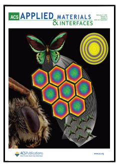

ACS Publications © 2021 American Chemical Society

https://dx.doi.org/10.1021/acsami.0c17947
ACS Appl. Mater. Interfaces 2021, 13, 4975−4983

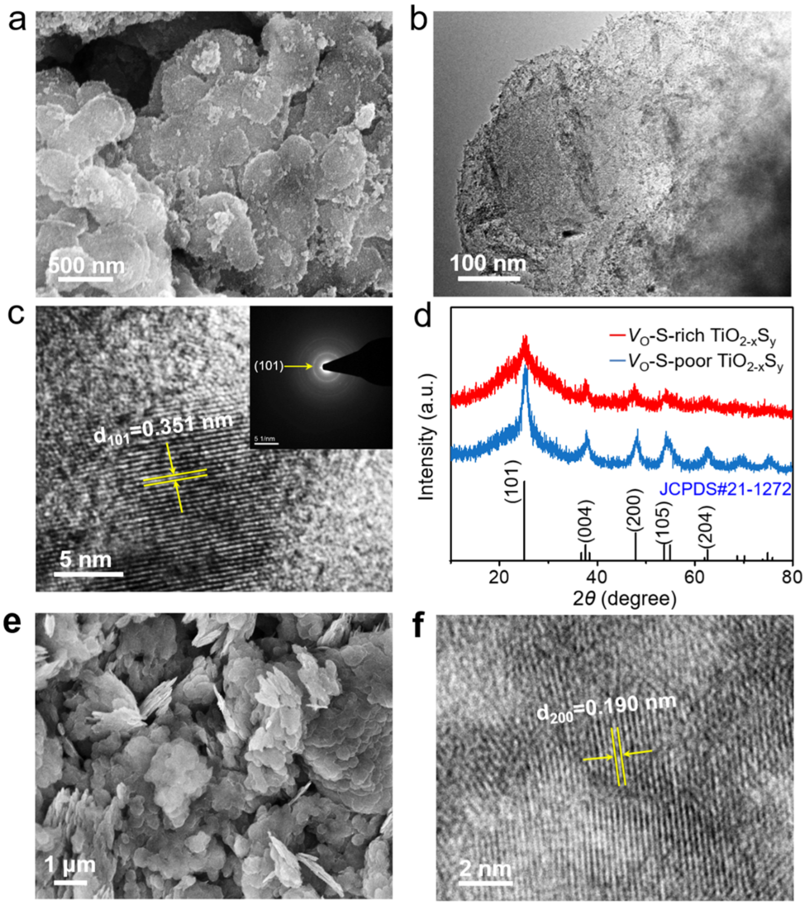

Figure 1. (a−c) SEM image, TEM image, and HRTEM image of V_O-S-rich $TiO_{2-x}S_y$ nanoplatelets. The inset in (c) is the corresponding SAED image. (d) XRD patterns of V_O-S-rich and V_O-S-poor $TiO_{2-x}S_y$ nanoplatelets. (e) SEM and (f) TEM images of V_O-S-poor $TiO_{2-x}S_y$ nanoplatelets, respectively.

induced electrons and holes.[20] Therefore, it is paramount to improve the optical absorption and inhibit the electron−hole recombination of TiO_2. Recently, the emergence of various black titania materials synthesized by different strategies has triggered a boom of research interests in photocatalytic field, owing to enhanced light absorption, promoted charge transport, and abundant active sites of black titania.[21−28] However, the modulation ranges of bandgap and electronic structure are still limited merely by introducing oxygen vacancies, and thus, the catalytic activity is not fully satisfactory. Therefore, we suggest that the energy band structure, light absorption properties, and surface-active sites of black TiO_2 can be further modulated by the dual strategy of introducing dopants and oxygen vacancies simultaneously.

In this work, ultrathin anatase nanoplatelets with abundant oxygen vacancies and sulfur dopants (V_O-S-rich $TiO_{2-x}S_y$) were successfully synthesized, achieving a significant enhancement on photocatalytic nitrogen fixation performance. The V_O-S-rich $TiO_{2-x}S_y$ nanoplatelets were prepared by an ion-exchange method with TiS_2 nanoplatelets as precursors under mild conditions and well maintained the morphologies and structures of precursor TiS_2 nanoplatelets. Meanwhile, beige $TiO_{2-x}S_y$ nanoplatelets with much fewer oxygen vacancies and sulfur dopants (V_O-S-poor $TiO_{2-x}S_y$) were also prepared as a control sample by subsequent air sintering. To investigate the synergistic effect of oxygen vacancies and sulfur doping, the photo-driven ammonia synthesis performances of V_O-S-rich $TiO_{2-x}S_y$, V_O-S-poor $TiO_{2-x}S_y$ nanoplatelets, and commercially available TiO_2 nanopowders (P25) are compared at ambient conditions in pure water without sacrificial regents. With the advantages of enhanced light absorption, effective photo-induced electron−hole separation, and more active sites, the V_O-S-rich $TiO_{2-x}S_y$ nanoplatelets exhibit an ammonia generation rate of 86.2 μmol g^{-1} h^{-1} under visible−NIR light irradiation, which remarkably outperforms that of V_O-S-poor $TiO_{2-x}S_y$ nanoplatelets (15.3 μmol g^{-1} h^{-1}). The V_O-S-rich $TiO_{2-x}S_y$ nanoplatelets also show a higher ammonia production rate of 114.1 μmol g^{-1} h^{-1} under full-spectrum light, which is almost 4 times that of V_O-S-poor $TiO_{2-x}S_y$ nanoplatelets (30.2 μmol g^{-1} h^{-1}). In contrast, commercial P25 shows very little ammonia generation under the same conditions, demonstrating the crucial role of oxygen vacancies and sulfur doping on photocatalytic N_2 fixation. Density functional theory (DFT) calculations are employed to interpret the improved photocatalytic activity of V_O-S-rich $TiO_{2-x}S_y$. The greatly enhanced adsorption and activation of N_2 molecules on the surface of V_O-S-rich $TiO_{2-x}S_y$ shed insights into the rational design of photocatalysts by defect engineering and elemental doping for the reduction of N_2 at room temperature and atmospheric pressure.

2. RESULTS AND DISCUSSION

The precursor TiS_2 nanoplatelets were prepared by a modified solvothermal process, as detailed in the Supporting Information. Powder X-ray diffraction (XRD) analysis was used to

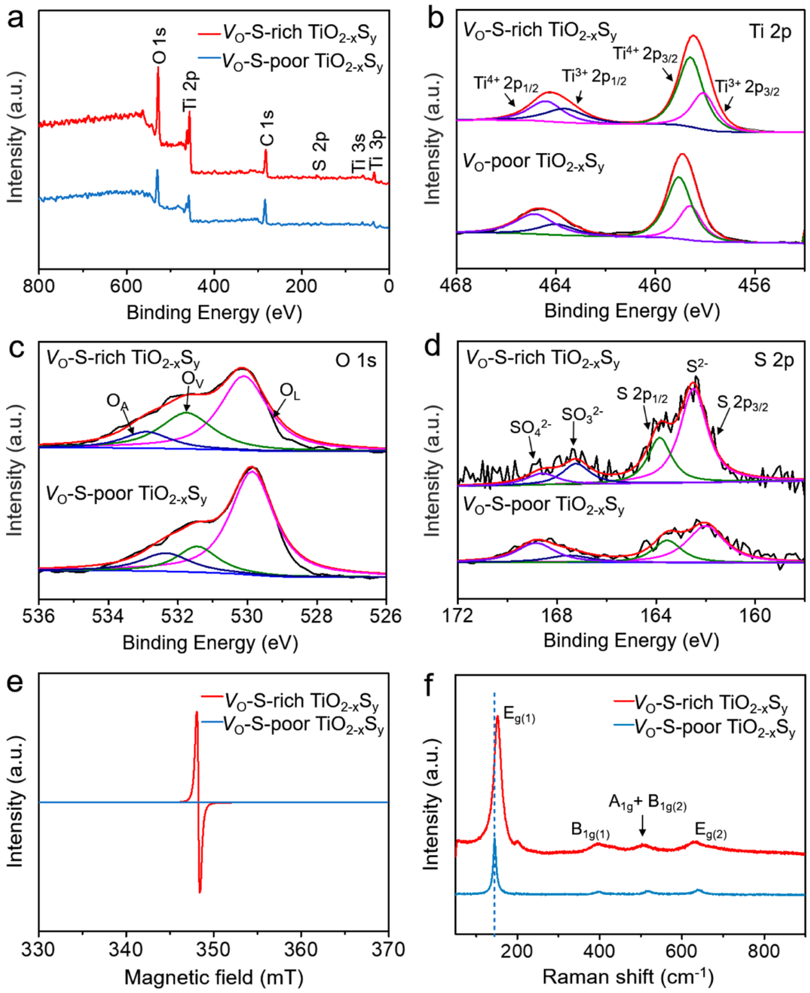

Figure 2. (a) Survey XPS spectra and high-resolution XPS spectra of (b) Ti 2p, (c) O 1s, and (d) S 2p regions of V_O-S-rich and V_O-S-poor $TiO_{2-x}S_y$ nanoplatelets, respectively. (e) EPR spectra (measured at room temperature) and (f) Raman spectra of V_O-S-rich and V_O-S-poor $TiO_{2-x}S_y$ nanoplatelets, respectively.

measure the crystallographic structure and phase purity of the precursor TiS_2 nanoplatelets (Figure S1a). All the diffraction peaks can be well assigned to hexagonal TiS_2 (JCPDS no. 15-0853) with no other miscellaneous peaks, suggesting the high purity. Scanning electron microscopy (SEM) and transmission electron microscopy (TEM) were employed to characterizing the morphologic features of precursor TiS_2, confirming the presence of nanoplatelets with a diameter of 300−400 nm (Figure S1b,c). From the high-resolution TEM image (HRTEM) in Figure S1d, the lattice fringes spacing of 0.109 nm is assigned to the (211) planes of the hexagonal TiS_2, and the selected area electron diffraction (SAED) patterns indicate the polycrystalline nature.

The V_O-S-rich $TiO_{2-x}S_y$ nanoplatelets were successfully synthesized by the slow hydrolysis of precursor TiS_2 nanoplatelets in the mixed solution of water and toluene under continuous stirring at 20 °C for 2 days. According to the previous reports, TiS_2 can be easily oxidized in the presence of water and O_2 to produce $TiS_{2-x}O_x$.[29,30] It is also known that a reducing atmosphere is required for the introduction of oxygen vacancies into TiO_2 via wet-chemical routes.[31] Therefore, we speculate that the reducing H_2S and SO_2 produced during the hydrolytic process of TiS_2 play a role in the formation of oxygen vacancies in $TiO_{2-x}S_y$ nanoplatelets. The morphology of the as-prepared V_O-S-rich $TiO_{2-x}S_y$ nanoplatelets are presented in Figure 1a,b. The product displays flake-like structures with a diameter of 300−400 nm and a rough surface. The HRTEM image of V_O-S-rich $TiO_{2-x}S_y$ nanoplatelets (Figure 1c) presents crystalline lattices with an interplanar spacing of 0.351 nm corresponding to the (101) planes of anatase-phase titania. The SAED pattern confirms the polycrystalline structure of V_O-S-rich $TiO_{2-x}S_y$ nanoplatelets. As a control sample, the V_O-S-poor $TiO_{2-x}S_y$ nanoplatelets were obtained by directly sintering precursor TiS_2 nanoplatelets at 400 °C in air. The successful formation of titania was confirmed by XRD analysis (Figure 1d). The diffraction peaks can be well indexed to anatase-phase titania (JCPDS NO. 21-1272). The XRD peaks of V_O-S-poor $TiO_{2-x}S_y$ nanoplatelets are stronger and sharper than those of V_O-S-rich $TiO_{2-x}S_y$ nanoplatelets, indicating the better crystallinity of V_O-S-poor $TiO_{2-x}S_y$ nanoplatelets induced by the high-temperature annealing. As shown in Figure 1e, the V_O-S-poor $TiO_{2-x}S_y$ sample also shows a similar nanoplatelet structure. The lattice distance in the Figure 1f is 0.19 nm corresponding to the (200) planes of anatase-phase titania.

The chemical compositions of V_O-S-rich and V_O-S-poor $TiO_{2-x}S_y$ nanoplatelets were investigated by XPS spectra. The survey XPS spectra in Figure 2a reveal the presence of Ti, O, and S elements. To further investigate the surface chemical states of the obtained samples, high-resolution XPS spectra at

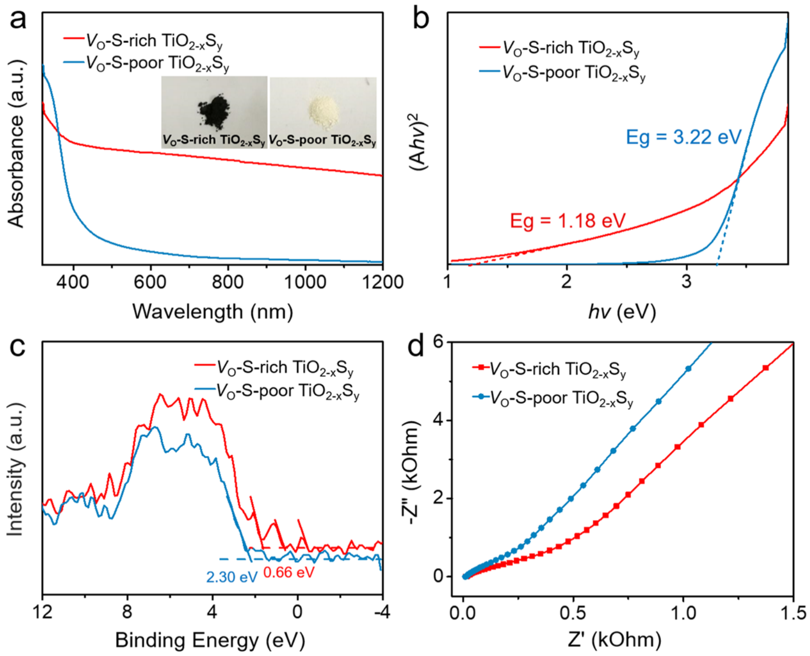

Figure 3. (a) Diffuse reflectance absorption spectra of V_O-S-rich and V_O-S-poor $TiO_{2-x}S_y$ nanoplatelets in the wavelength range between 300 and 1200 nm. (b) The Tauc plots of $(Ahv)^2$ *vs* photon energy for the bandgap deduction and (c) valence-band XPS spectra of V_O-S-rich and V_O-S-poor $TiO_{2-x}S_y$ nanoplatelets, respectively. (d) Electrochemical impedance spectra at 0.30 V *vs* reversible hydrogen electrode (RHE) in 0.5 mol L^{-1} Na_2SO_4 aqueous solutions under a 300 W Xe lamp without a cutoff filter.

Ti 2p, O 1s, and S 2p regions are presented in Figure 2b−d, which are calibrated by C 1s peak located at 284.6 eV. The Ti $2p_{3/2}$ and Ti $2p_{1/2}$ peaks centered at approximately 458.6 and 464.4 eV are ascribed to Ti^{4+}, and the peaks centered at approximately 458.1 and 463.7 eV are ascribed to Ti^{3+} (Figure 2b).[32] The O 1s core-level spectra (in Figure 2c) show three peaks located at 529.9, 531.7, and 532.9 eV, which can be attributed to the Ti−O−Ti bonds (lattice oxygen, O_L), the O-atoms in the vicinity of an oxygen vacancy (O_V), and the adsorbed O-atoms (O_A) on the surface of samples.[21,33] Notably, the binding energies of Ti species in V_O-S-rich $TiO_{2-x}S_y$ nanoplatelets are lower than those of V_O-S-poor $TiO_{2-x}S_y$, and the O_V peak intensity of V_O-S-rich $TiO_{2-x}S_y$ nanoplatelets is much stronger than that of V_O-S-poor $TiO_{2-x}S_y$ nanoplatelets, indicating the presence of much more oxygen vacancies in the former sample. In addition, Figure 2d shows the XPS spectra at the S 2p region of the as-prepared samples. The peaks located at 161.0−163.0 eV are assigned to the doping S^{2-} species,[34−37] and the weak peaks at 168.0−169.0 and 167.0−168.0 eV indicate the presence of small amounts of SO_4^{2-} and SO_3^{2-} derived from the slight surface oxidation, respectively. It is obvious that the concentration of S^{2-} species in V_O-S-rich $TiO_{2-x}S_y$ is much higher than that in V_O-S-poor $TiO_{2-x}S_y$, indicating more anionic sulfur doping in V_O-S-rich $TiO_{2-x}S_y$.

The presence of oxygen vacancies in the as-synthesized samples was further investigated by electron paramagnetic resonance (EPR) spectroscopy, which is used to examine unpaired electrons in materials. As presented in Figure 2e, the EPR spectrum of V_O-S-rich $TiO_{2-x}S_y$ nanoplatelets shows a strong signal at the *g*-value of 2.001 corresponding to the unpaired electrons trapped by oxygen vacancies.[38−40] In contract, there is almost no detectable EPR signal observed in V_O-S-poor $TiO_{2-x}S_y$. In addition, the Raman spectra of V_O-S-rich and V_O-S-poor $TiO_{2-x}S_y$ nanoplatelets were also obtained. As shown in Figure 2f, the V_O-S-poor $TiO_{2-x}S_y$ nanoplatelets exhibit four characteristic peaks at about 144.8, 398.9, 515.7, and 639.6 cm^{-1}, which are assigned to the Raman-active vibrational modes of $E_{g(1)}$, $B_{1g(1)}$, A_{1g} + $B_{1g(2)}$, and $E_{g(2)}$ bands, respectively.[41,42] Notably, the Raman spectrum of V_O-S-rich $TiO_{2-x}S_y$ nanoplatelets displays a clear blue shift, which can be ascribed to the generation of oxygen vacancies.[43,44] Nitrogen adsorption/desorption isotherms were used to investigate the specific surface area and porous structure of the as-prepared products. As displayed in Figure S2a,c,e, the BET surface areas of V_O-S-rich and V_O-S-poor $TiO_{2-x}S_y$ nanoplatelets are calculated to be 101 and 68 m^2 g^{-1}, respectively, which are higher than that of TiS_2 (49 m^2 g^{-1}). According to the Barrett−Joyner−Halenda (BJH) pore size distribution profiles (Figure S2b,d,f), V_O-S-rich and V_O-S-poor $TiO_{2-x}S_y$ nanoplatelets exhibit obvious micro-mesoporous structures with the diameters distributed in the range of 1−10 nm. These porous channels are anticipated to be beneficial for the photocatalytic N_2 fixation reaction by providing more active sites.

The UV−visible diffuse reflectance absorption spectra of V_O-S-rich $TiO_{2-x}S_y$ and V_O-S-poor $TiO_{2-x}S_y$ nanoplatelets are shown in Figure 3a. Compared with V_O-S-poor $TiO_{2-x}S_y$ nanoplatelets, the light absorption range of V_O-S-rich $TiO_{2-x}S_y$ nanoplatelets is significantly extended from about 400 nm to the NIR region. The V_O-S-rich $TiO_{2-x}S_y$ nanoplatelets exhibit a broader and stronger absorption tail from ∼450 nm to the NIR region, which thus endows V_O-S-rich $TiO_{2-x}S_y$ black color, while the V_O-S-poor $TiO_{2-x}S_y$ displays beige color. The substantial light absorption enhancement of V_O-S-rich $TiO_{2-x}S_y$ nanoplatelets in the visible and NIR regions should be attributed to the impurity mid-gaps induced by oxygen vacancies and sulfur dopants.[21,35,45] The corresponding bandgap of V_O-S-rich $TiO_{2-x}S_y$ nanoplatelets estimated from the Tauc plots (Figure 3b) is 1.18 eV, much smaller than the

https://dx.doi.org/10.1021/acsami.0c17947
ACS Appl. Mater. Interfaces 2021, 13, 4975−4983

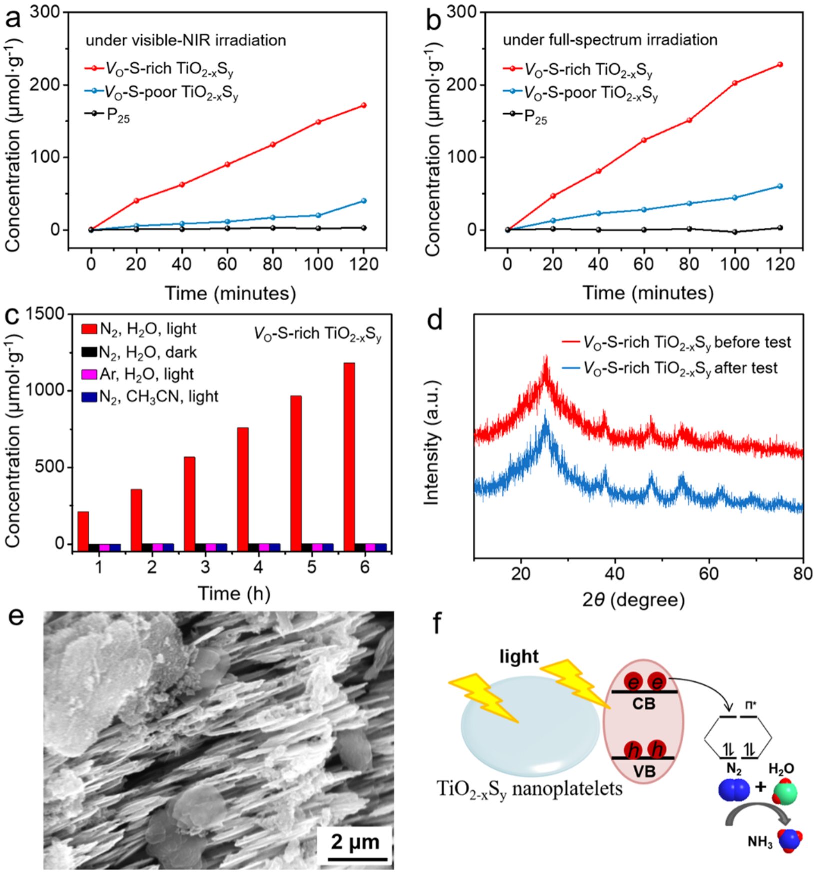

Figure 4. (a,b) The ammonia yields of V_O-S-rich $TiO_{2-x}S_y$, V_O-S-poor $TiO_{2-x}S_y$ nanoplatelets, and P25 photocatalysts over the test period of 2 h under (a) visible−NIR irradiation (with a 420 nm cutoff filter) and (b) full-spectrum light irradiation (without a cutoff filter) in ultrapure water under continuous N_2 bubbling at room temperature and ambient pressure. (c) Catalyst cycling tests of V_O-S-rich $TiO_{2-x}S_y$ nanoplatelets under different conditions (without a cutoff filter). (d) XRD patterns and (e) SEM images of V_O-S-rich $TiO_{2-x}S_y$ nanoplatelets after photocatalytic nitrogen fixation test for 2 h under full-spectrum irradiation (without cutoff filter). (f) A proposed schematic illustration of the photocatalytic N_2 fixation process on $TiO_{2-x}S_y$ nanoplatelets.

bandgap of V_O-S-poor $TiO_{2-x}S_y$ (E_g = 3.22 eV). This result indicates that the co-presence of oxygen vacancies and sulfur dopants in titania can greatly change the band structure and form abundant defect energy levels and impurity energy levels, leading to the extension of light absorption within the visible and NIR regions. The valence bands of both samples were also measured by valence band XPS spectra (Figure 3c). Figure 3c shows that the valence band maximums of V_O-S-poor $TiO_{2-x}S_y$ and V_O-S-rich $TiO_{2-x}S_y$ are located at 2.3 and 0.66 eV below the Fermi level, respectively. It is notable that some sublevels emerge near the Fermi level in the valence band XPS spectra, which can be ascribed to the impurity and defect band levels.[46,47] The synergistic effect of oxygen vacancies and sulfur doping on the photogenerated carrier separation and transport was investigated by the Nyquist plots (Figure 3d) measured by electrochemical impedance spectroscopy. Compared with V_O-S-poor $TiO_{2-x}S_y$, the V_O-S-rich $TiO_{2-x}S_y$ sample displays a greatly decreased charge-transfer resistance resulted from the narrower bandgap and higher defect/impurity carrier concentration induced by the oxygen vacancies and sulfur doping.[40]

To disclose the role of oxygen vacancies and sulfur doping in affecting photocatalysis, the photocatalytic nitrogen reduction reaction was conducted on V_O-S-rich $TiO_{2-x}S_y$, V_O-S-poor $TiO_{2-x}S_y$ and commercial P25 under ambient conditions in water without any sacrificial reagents or cocatalysts. As shown in Figure 4a, under visible−NIR irradiation of a 300 W Xe lamp with 420 nm cutoff filter, the V_O-S-rich and V_O-S-poor $TiO_{2-x}S_y$ nanoplatelets exhibit the ammonia generation rates of 86.2 and 15.3 μmol g^{-1} h^{-1}, respectively. Under full-spectrum light (300 W Xe lamp without cutoff filter), the ammonia yield rates of V_O-S-rich and V_O-S-poor $TiO_{2-x}S_y$ nanoplatelets are measured to be 114.1 and 30.2 μmol g^{-1} h^{-1}, respectively (Figure 4b). The photocatalytic N_2 fixation rate of V_O-S-rich $TiO_{2-x}S_y$ under full-spectrum light was also evaluated by ion chromatography (Figure S4) and the ammonia production rate was measured to be 110 μmol g^{-1} h^{-1}, which is comparable to the yield of ammonia quantified by the colorimetric method. Remarkably, commercial P25 delivers a very little ammonia yield at the same conditions. As summarized in Table S1, the photocatalytic N_2 fixation performance of V_O-S-rich $TiO_{2-x}S_y$ nanoplatelets is competitive among the reported photocatalysts.

To identify the NIR responsibility of black $TiO_{2-x}S_y$ nanoplatelets, photocatalytic N_2 fixation test was also performed with a cutoff filter of 800 nm wavelength, which can apply the illumination of mere NIR light within the range between 800 and 1100 nm. Remarkably, the V_O-S-rich $TiO_{2-x}S_y$ nanoplatelets can still deliver an ammonia generation rate of 14.1 μmol g^{-1} h^{-1} under only NIR irradiation, as presented in Figure S5. This is mainly because the oxygen vacancies and sulfur doping can narrow the bandgap to enhance the light absorption that can even reach the NIR

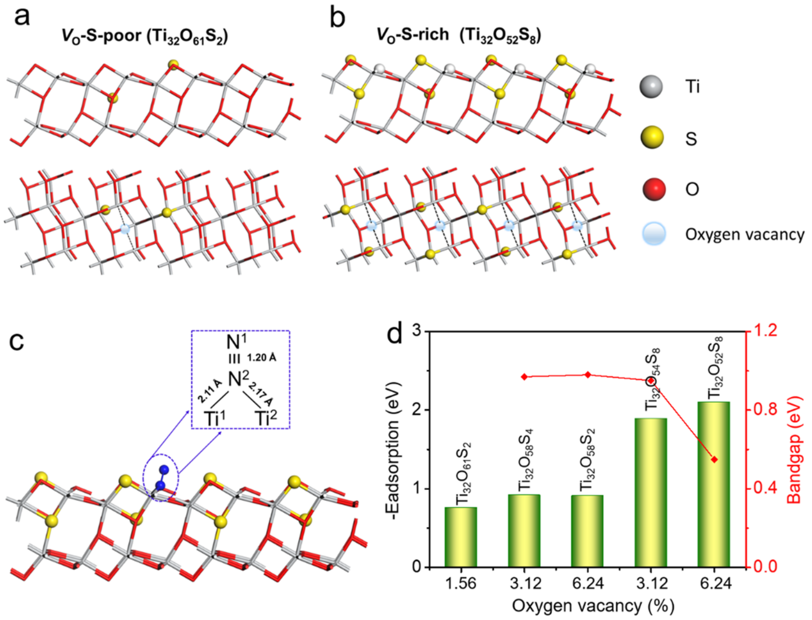

Figure 5. (a,b) Front view (top) and top view (bottom) of the simulated slab models of (a) V_O-S-rich ($Ti_{32}O_{52}S_8$)-(101) surface and (b) V_O-S-poor ($Ti_{32}O_{61}S_2$)-(101) surface with the sulfur dopants on the cross. (c) The pristine surface model with N_2 (end-on structure) adsorbed at $Ti_{32}O_{52}S_8$. (d) The synergistic effect of different contents of oxygen vacancies and sulfur anion dopants on the bandgap and adsorption energy.

region. Moreover, the presence of oxygen vacancies and sulfur dopants in titania also provide more active sites to facilitate the separation of photo-induced electrons and holes, thus plays a decisive role in the photocatalytic N_2 fixation reaction. According to previous studies,[48−51] the oxygen vacancies as electron traps can efficiently inhibit the recombination of photogenerated electrons and holes and be conducive to the adsorption and activation of inert N_2 molecules.

The performance stability of V_O-S-rich $TiO_{2-x}S_y$ nanoplatelets for photocatalytic nitrogen fixation was also investigated under full-spectrum light irradiation, showing almost no decrease in ammonia yield after six successive photocatalytic cycles, as shown in Figure 4c. Furthermore, control experiments in the absence of N_2, H_2O or light illumination were also performed, and no ammonia was detected (Figure 4c). These results indicate that the N_2, H_2O, and light irradiation are essential to the photocatalytic nitrogen fixation, and the nitrogen and proton resource of the produced ammonia are originated from N_2 and H_2O, respectively, rather than from other possible sources or impurities. What is more, XRD and SEM measurements (Figure 4d,e) show that crystalline structure and morphologic features of V_O-S-rich $TiO_{2-x}S_y$ nanoplatelets have no obvious change after 2 h testing, further confirming the photocatalytic stability of V_O-S-rich $TiO_{2-x}S_y$ nanoplatelets.

A possible photocatalytic N_2 fixation process on $TiO_{2-x}S_y$ was illustrated in Figure 4f. After the adsorption of N_2 molecules on the surface of photocatalyst, the photoexcited electrons were generated upon light irradiation and migrated to the surface of the photocatalyst. Subsequently, the photogenerated electrons were transferred to the empty π anti-bonding orbitals (π^*) of the N_2 molecules, activating the N_2 molecules. As expected, the length of N≡N bonds was gradually increased, and the N_2 molecules were stepwisely hydrogenated and then dissociated, producing NH_3 molecules. Finally, the generated ammonia molecules were desorbed on the photocatalyst surface. Theoretical calculations were also conducted to investigate the synergistic effect of different contents of oxygen vacancies and sulfur doping on N_2 photofixation. As presented in Figure 5a,b, the slab models were built for the simulation of V_O-S-rich $TiO_{2-x}S_y$ (represented by $Ti_{32}O_{52}S_8$, with four oxygen vacancies and eight sulfur atoms in each slab) and V_O-S-poor $TiO_{2-x}S_y$ (represented by $Ti_{32}O_{61}S_2$, with one oxygen vacancy and two sulfur atoms in each slab), respectively. Figure 5c displays the relative strength of N_2 molecule adsorption on the $TiO_{2-x}S_y$-(101) surfaces with different contents of oxygen vacancies and S dopants. With the increase of oxygen vacancy and sulfur anion concentrations, the adsorption energy changes significantly from −0.76 to −2.1 eV, indicating that the N_2 adsorption on V_O-S-rich $TiO_{2-x}S_y$ is energetically more favorable than that on V_O-S-poor $TiO_{2-x}S_y$. Besides, to investigate the sulfur doping positions in $TiO_{2-x}S_y$-(101), another slab model was built with the predominant sulfur doping located on the top (Figure S6), which is thermodynamically more stable than the slab model with the sulfur dopants on the cross. As shown in Table S2, the $TiO_{2-x}S_y$-(101) slab model with the sulfur dopants on the top shows the smaller energy difference than the lab model with the sulfur dopants on the cross (0.53 eV), indicating that the sulfur dopants on the top are markedly beneficial to the nitrogen photofixation reaction. The energy bands of $TiO_{2-x}S_y$-(101) slab models with different oxygen vacancy and sulfur anion dopant ratios were also calculated, as shown in Figure S7. According to Figure S7, when the concentration of oxygen vacancies is the same, the more the sulfur dopants, the narrower the bandgap ($2V_O$ + 4S: 0.97 eV; $2V_O$ + 8S: 0.95 eV; $4V_O$ + 2S: 0.98 eV; and $4V_O$ + 8S: 0.55 eV). On the other hand, when the sulfur dopants are the same, the more the oxygen vacancies, the narrower the bandgap ($2V_O$ + 8S: 0.95 eV; $4V_O$ + 8S: 0.55 eV). These results indicate that the oxygen vacancies and sulfur dopants can jointly promote the narrowing of bandgap. Figure 5d summarizes the effects of oxygen vacancies and sulfur anion dopants on the bandgap and

https://dx.doi.org/10.1021/acsami.0c17947

adsorption energy of N_2 molecule on different $TiO_{2-x}S_y$-(101) surfaces. It reveals that the co-presence of oxygen vacancies and sulfur dopants can greatly narrow the bandgap of titania and facilitate the adsorption of inert N_2, hence promoting the performance of photocatalytic nitrogen fixation. In a recent theoretical study, the photolysis of H_2O adsorbed on rutile (110) surface with oxygen vacancies was predicted to be able to drive the N_2 reduction to NH_3,[52] which is consistent with our results.

3. CONCLUSIONS

In summary, we have developed an efficient strategy to prepare *V*o-S-rich $TiO_{2-x}S_y$ nanoplatelets enriched with oxygen vacancies and sulfur dopants at mild conditions. The simultaneous introduction of oxygen vacancies and sulfur dopants are found to significantly extend the light response from ultraviolet to visible region and further to NIR region. The greatly enhanced light absorption is also advantageous to the utilization of solar power. In addition, the oxygen vacancies can serve as carrier traps to effectively inhibit the photogenerated electron−hole recombination and act as active sites for the nitrogen reduction reaction. DFT calculations demonstrated that the more oxygen vacancies and S dopants are introduced, the more easily N_2 molecules adsorb on the catalyst surface. Compared to the *V*o-S-poor $TiO_{2-x}S_y$ nanoplatelets, the *V*o-S-rich $TiO_{2-x}S_y$ nanoplatelets exhibit about 3.0 and 4.5 times higher photocatalytic activity for nitrogen fixation under visible−NIR and full-spectrum irradiations, respectively, owing to the synergistic effect of oxygen vacancies and sulfur doping. This work provides a promising route for developing advanced photocatalysts with rationally designed atomic structures, electronic properties, and interfaces toward N_2 photochemical reduction into ammonia.

■ ASSOCIATED CONTENT

Supporting Information

The Supporting Information is available free of charge at https://pubs.acs.org/doi/10.1021/acsami.0c17947.

> XRD patterns, SEM images, TEM images, and HRTEM images; nitrogen adsorption−desorption isotherms; standard calibration curve; ammonia yield; simulated slab models; computed band structures and bandgaps; performance comparison; and calculated total energy (PDF)

■ AUTHOR INFORMATION

Corresponding Authors

Jing Ma − *MOE Key Laboratory of Mesoscopic Chemistry, MOE Key Laboratory of High Performance Polymer Materials and Technology, Jiangsu Key Laboratory of Advanced Organic Materials, School of Chemistry and Chemical Engineering, Nanjing University, Nanjing 210023, China;* orcid.org/0000-0001-5848-9775; Email: majing@nju.edu.cn

Zhong Jin − *MOE Key Laboratory of Mesoscopic Chemistry, MOE Key Laboratory of High Performance Polymer Materials and Technology, Jiangsu Key Laboratory of Advanced Organic Materials, School of Chemistry and Chemical Engineering, Nanjing University, Nanjing 210023, China; Shenzhen Research Institute of Nanjing University, Shenzhen 518057, China;* orcid.org/0000-0001-8860-8579; Email: zhongjin@nju.edu.cn

Authors

Xiaolan Xue − *MOE Key Laboratory of Mesoscopic Chemistry, MOE Key Laboratory of High Performance Polymer Materials and Technology, Jiangsu Key Laboratory of Advanced Organic Materials, School of Chemistry and Chemical Engineering, Nanjing University, Nanjing 210023, China*

Hongwei Chen − *MOE Key Laboratory of Mesoscopic Chemistry, MOE Key Laboratory of High Performance Polymer Materials and Technology, Jiangsu Key Laboratory of Advanced Organic Materials, School of Chemistry and Chemical Engineering, Nanjing University, Nanjing 210023, China*

Yan Xiong − *MOE Key Laboratory of Mesoscopic Chemistry, MOE Key Laboratory of High Performance Polymer Materials and Technology, Jiangsu Key Laboratory of Advanced Organic Materials, School of Chemistry and Chemical Engineering, Nanjing University, Nanjing 210023, China*

Renpeng Chen − *MOE Key Laboratory of Mesoscopic Chemistry, MOE Key Laboratory of High Performance Polymer Materials and Technology, Jiangsu Key Laboratory of Advanced Organic Materials, School of Chemistry and Chemical Engineering, Nanjing University, Nanjing 210023, China*

Minghang Jiang − *MOE Key Laboratory of Mesoscopic Chemistry, MOE Key Laboratory of High Performance Polymer Materials and Technology, Jiangsu Key Laboratory of Advanced Organic Materials, School of Chemistry and Chemical Engineering, Nanjing University, Nanjing 210023, China*

Gao Fu − *MOE Key Laboratory of Mesoscopic Chemistry, MOE Key Laboratory of High Performance Polymer Materials and Technology, Jiangsu Key Laboratory of Advanced Organic Materials, School of Chemistry and Chemical Engineering, Nanjing University, Nanjing 210023, China*

Zhonghua Xi − *MOE Key Laboratory of Mesoscopic Chemistry, MOE Key Laboratory of High Performance Polymer Materials and Technology, Jiangsu Key Laboratory of Advanced Organic Materials, School of Chemistry and Chemical Engineering, Nanjing University, Nanjing 210023, China*

Xiao Li Zhang − *School of Materials Science and Engineering, Zhengzhou University, Zhengzhou 450001, China*

Weihai Fang − *MOE Key Laboratory of Mesoscopic Chemistry, MOE Key Laboratory of High Performance Polymer Materials and Technology, Jiangsu Key Laboratory of Advanced Organic Materials, School of Chemistry and Chemical Engineering, Nanjing University, Nanjing 210023, China; Key Laboratory of Theoretical and Computational Photochemistry, Ministry of Education, College of Chemistry, Beijing Normal University, Beijing 100875, China;* orcid.org/0000-0002-1668-465X

Complete contact information is available at: https://pubs.acs.org/10.1021/acsami.0c17947

Author Contributions

$^{\perp}$X.X. and H.C. contributed equally to this work.

Notes

The authors declare no competing financial interest.

■ ACKNOWLEDGMENTS

This work was supported by the National Key Research and Development Program of China (2017YFA0208200 and 2016YFB0700600), the Fundamental Research Funds for the Central Universities of China (0205-14380219), the Projects of NSFC (22022505, 21872069, and 51761135104), the Natural Science Foundation of Jiangsu Province (BK20180008), and the High-Level Innovation and Entrepreneurship Project of Jiangsu Province of China.

■ REFERENCES

(1) Galloway, J. N.; Townsend, A. R.; Erisman, J. W.; Bekunda, M.; Cai, Z.; Freney, J. R.; Martinelli, L. A.; Seitzinger, S. P.; Sutton, M. A. Transformation of the Nitrogen Cycle: Recent Trends, Questions, and Potential Solutions. *Science* **2008**, *320*, 889−892.

(2) Tanaka, H.; Nishibayashi, Y.; Yoshizawa, K. Interplay between Theory and Experiment for Ammonia Synthesis Catalyzed by Transition Metal Complexes. *Acc. Chem. Res.* **2016**, *49*, 987−995.

(3) Klerke, A.; Christensen, C. H.; Nørskov, J. K.; Vegge, T. Ammonia for Hydrogen Storage: Challenges and Opportunities. *J. Mater. Chem.* **2008**, *18*, 2304−2310.

(4) Lan, R.; Irvine, J. T. S.; Tao, S. Ammonia and Related Chemicals as Potential Indirect Hydrogen Storage Materials. *Int. J. Hydrogen Energy* **2012**, *37*, 1482−1494.

(5) Li, L.; Wang, Y.; Vanka, S.; Mu, X.; Mi, Z.; Li, C.-J. Nitrogen Photofixation over III-Nitride Nanowires Assisted by Ruthenium Clusters of Low Atomicity. *Angew. Chem., Int. Ed.* **2017**, *56*, 8701−8705.

(6) Shilov, A. E. Catalytic Reduction of Molecular Nitrogen in Solutions. *Russ. Chem. Bull.* **2003**, *52*, 2555−2562.

(7) Keane, A. J.; Zavalij, P. Y.; Sita, L. R. N−N Bond Cleavage of Mid-valent Ta (IV) Hydrazido and Hydrazidium Complexes Relevant to the Schrock Cycle for Dinitrogen Fixation. *J. Am. Chem. Soc.* **2013**, *135*, 9580−9583.

(8) Kandemir, T.; Schuster, M. E.; Senyshyn, A.; Behrens, M.; Schlögl, R. The Haber−Bosch Process Revisited: on the Real Structure and Stability of "Ammonia Iron" under Working Conditions. *Angew. Chem., Int. Ed.* **2013**, *52*, 12723−12726.

(9) Shipman, M. A.; Symes, M. D. Recent Progress towards the Electrosynthesis of Ammonia from Sustainable Resources. *Catal. Today* **2017**, *286*, 57−68.

(10) Rafiqul, I.; Weber, C.; Lehmann, B.; Voss, A. Energy Efficiency Improvements in Ammonia Production−Perspectives and Uncertainties. *Energy* **2005**, *30*, 2487−2504.

(11) Tanabe, Y.; Nishibayashi, Y. Developing More Sustainable Processes for Ammonia Synthesis. *Coord. Chem. Rev.* **2013**, *257*, 2551−2564.

(12) Medford, A. J.; Hatzell, M. C. Photon-Driven Nitrogen Fixation: Current Progress, Thermodynamic Considerations, and Future Outlook. *ACS Catal.* **2017**, *7*, 2624−2643.

(13) Chen, X.; Li, N.; Kong, Z.; Ong, W.-J.; Zhao, X. Photocatalytic Fixation of Nitrogen to Ammonia: State-of-the-Art Advancements and Future Prospects. *Mater. Horiz.* **2018**, *5*, 9−27.

(14) Schrauzer, G. N.; Guth, T. D. Photolysis of Water and Photoreduction of Nitrogen on Titanium Dioxide. *J. Am. Chem. Soc.* **1977**, *99*, 7189−7193.

(15) Soria, J.; Conesa, J. C.; Augugliaro, V.; Palmisano, L.; Schiavello, M.; Sclafani, A. Dinitrogen Photoreduction to Ammonia over Titanium Dioxide Powders Doped with Ferric Ions. *J. Phys. Chem.* **1991**, *95*, 274−282.

(16) Rao, N. N.; Dube, S.; Manjubala, P.; Natarajan, P. Photocatalytic Reduction of Nitrogen over (Fe, Ru or Os)/TiO_2 Catalysts. *Appl. Catal. B Environ.* **1994**, *5*, 33−42.

(17) Ranjit, K. T.; Varadarajan, T. K.; Viswanathan, B. Photocatalytic Reduction of Dinitrogen to Ammonia over Noble-Metal-Loaded TiO_2. *J. Photochem. Photobiol., A* **1996**, *96*, 181−185.

(18) Zhao, W.; Zhang, J.; Zhu, X.; Zhang, M.; Tang, J.; Tan, M.; Wang, Y. Enhanced Nitrogen Photofixation on Fe-Doped TiO_2 with Highly Exposed (101) Facets in the Presence of Ethanol as Scavenger. *Appl. Catal. B Environ.* **2014**, *144*, 468−477.

(19) Hirakawa, H.; Hashimoto, M.; Shiraishi, Y.; Hirai, T. Photocatalytic Conversion of Nitrogen to Ammonia with Water on Surface Oxygen Vacancies of Titanium Dioxide. *J. Am. Chem. Soc.* **2017**, *139*, 10929−10936.

(20) Chen, X.; Liu, L.; Huang, F. Black Titanium Dioxide (TiO_2) Nanomaterials. *Chem. Soc. Rev.* **2015**, *44*, 1861−1885.

(21) Liu, X.; Zhu, G.; Wang, X.; Yuan, X.; Lin, T.; Huang, F. Progress in Black Titania: a New Material for Advanced Photocatalysis. *Adv. Energy Mater.* **2016**, *6*, 1600452.

(22) Chen, X.; Liu, L.; Yu, P. Y.; Mao, S. S. Increasing Solar Absorption for Photocatalysis with Black Hydrogenated Titanium Dioxide Nanocrystals. *Science* **2011**, *331*, 746−750.

(23) Liu, N.; Schneider, C.; Freitag, D.; Hartmann, M.; Venkatesan, U.; Müller, J.; Spiecker, E.; Schmuki, P. Black TiO_2 Nanotubes: Cocatalyst-Free Open-Circuit Hydrogen Generation. *Nano Lett.* **2014**, *14*, 3309−3313.

(24) Tian, M.; Mahjouri-Samani, M.; Eres, G.; Sachan, R.; Yoon, M.; Chisholm, M. F.; Wang, K.; Puretzky, A. A.; Rouleau, C. M.; Geohegan, D. B.; Duscher, G. Structure and Formation Mechanism of Black TiO_2 Nanoparticles. *ACS Nano* **2015**, *9*, 10482−10488.

(25) Wang, Z.; Yang, C.; Lin, T.; Yin, H.; Chen, P.; Wan, D.; Xu, F.; Huang, F.; Lin, J.; Xie, X.; Jiang, M. Visible-Light Photocatalytic, Solar Thermal and Photoelectrochemical Properties of Aluminium-Reduced Black Titania. *Energy Environ. Sci.* **2013**, *6*, 3007−3014.

(26) Sinhamahapatra, A.; Jeon, J.-P.; Yu, J.-S. A New Approach to Prepare Highly Active and Stable Black Titania for Visible Light-Assisted Hydrogen Production. *Energy Environ. Sci.* **2015**, *8*, 3539−3544.

(27) Zou, X.; Liu, J.; Su, J.; Zuo, F.; Chen, J.; Feng, P. Facile Synthesis of Thermal- and Photostable Titania with Paramagnetic Oxygen Vacancies for Visible-Light Photocatalysis. *Chem.—Eur. J.* **2013**, *19*, 2866−2873.

(28) Zuo, F.; Wang, L.; Wu, T.; Zhang, Z.; Borchardt, D.; Feng, P. Self-Doped Ti^{3+} Enhanced Photocatalyst for Hydrogen Production under Visible Light. *J. Am. Chem. Soc.* **2010**, *132*, 11856−11857.

(29) Cucinotta, C. S.; Dolui, K.; Pettersson, H.; Ramasse, Q. M.; Long, E.; O'Brian, S. E.; Nicolosi, V.; Sanvito, S. Electronic Properties and Chemical Reactivity of TiS_2 Nanoflakes. *J. Phys. Chem. C* **2015**, *119*, 15707−15715.

(30) Long, E.; O'Brien, S.; Lewis, E. A.; Prestat, E.; Downing, C.; Cucinotta, C. S.; Sanvito, S.; Haigh, S. J.; Nicolosi, V. An in situ and ex situ TEM Study into the Oxidation of Titanium (IV) Sulphide. *npj 2D Mater. Appl.* **2017**, *1*, 22.

(31) Sarkar, A.; Khan, G. G. The Formation and Detection Techniques of Oxygen Vacancies in Titanium Oxide-Based Nanostructures. *Nanoscale* **2019**, *11*, 3414−3444.

(32) Liu, X.; Xing, Z.; Zhang, H.; Wang, W.; Zhang, Y.; Li, Z.; Wu, X.; Yu, X.; Zhou, W. Fabrication of 3D Mesoporous Black TiO_2/MoS_2/TiO_2 Nanosheets for Visible-Light-Driven Photocatalysis. *ChemSusChem* **2016**, *9*, 1118−1124.

(33) Gao, S.; Sun, Z.; Liu, W.; Jiao, X.; Zu, X.; Hu, Q.; Sun, Y.; Yao, T.; Zhang, W.; Wei, S.; Xie, Y. Atomic Layer Confined Vacancies for Atomic-Level Insights into Carbon Dioxide Electroreduction. *Nat. Commun.* **2017**, *8*, 14503.

(34) Lee, H. U.; Lee, S. C.; Choi, S. H.; Son, B.; Lee, S. J.; Kim, H. J.; Lee, J. Highly Visible-Light Active Nanoporous TiO_2 Photocatalysts for Efficient Solar Photocatalytic Applications. *Appl. Catal. B Environ.* **2013**, *129*, 106−113.

(35) Ni, J.; Fu, S.; Wu, C.; Maier, J.; Yu, Y.; Li, L. Self-Supported Nanotube Arrays of Sulfur-Doped TiO_2 Enabling Ultrastable and Robust Sodium Storage. *Adv. Mater.* **2016**, *28*, 2259−2265.

(36) Zhu, M.; Zhai, C.; Qiu, L.; Lu, C.; Paton, A. S.; Du, Y.; Goh, M. C. New Method to Synthesize S-Doped TiO_2 with Stable and Highly Efficient Photocatalytic Performance under Indoor Sunlight Irradiation. *ACS Sustain. Chem. Eng.* **2015**, *3*, 3123−3129.

(37) Rengifo-Herrera, J. A.; Mielczarski, E.; Mielczarski, J.; Castillo, N. C.; Kiwi, J.; Pulgarin, C. Escherichia coli inactivation by N, S co-doped commercial TiO2 powders under UV and visible light. *Appl. Catal. B Environ.* **2008**, *84*, 448−456.

(38) Chong, S. V.; Kadowaki, K.; Xia, J.; Idriss, H. Interesting Magnetic Behavior from Reduced Titanium Dioxide Nanobelts. *Appl. Phys. Lett.* **2008**, *92*, 232502.

(39) Lin, T.; Yang, C.; Wang, Z.; Yin, H.; Lü, X.; Huang, F.; Lin, J.; Xie, X.; Jiang, M. Effective Nonmetal Incorporation in Black Titania with Enhanced Solar Energy Utilization. *Energy Environ. Sci.* **2014**, *7*, 967−972.

(40) Zhang, Y.; Ding, Z.; Foster, C. W.; Banks, C. E.; Qiu, X.; Ji, X. Oxygen Vacancies Evoked Blue TiO_2 (B) Nanobelts with Efficiency Enhancement in Sodium Storage Behaviors. *Adv. Funct. Mater.* **2017**, *27*, 1700856.

(41) Pan, X.; Yang, M.-Q.; Fu, X.; Zhang, N.; Xu, Y.-J. Defective TiO_2 with Oxygen Vacancies: Synthesis, Properties and Photocatalytic Applications. *Nanoscale* **2013**, *5*, 3601−3614.

(42) Zhang, J.; Yu, Z.; Gao, Z.; Ge, H.; Zhao, S.; Chen, C.; Chen, S.; Tong, X.; Wang, M.; Zheng, Z.; Qin, Y. Porous TiO_2 Nanotubes with Spatially Separated Platinum and CoO_x Cocatalysts Produced by Atomic Layer Deposition for Photocatalytic Hydrogen Production. *Angew. Chem., Int. Ed.* **2017**, *56*, 816−820.

(43) Naldoni, A.; Allieta, M.; Santangelo, S.; Marelli, M.; Fabbri, F.; Cappelli, S.; Bianchi, C. L.; Psaro, R.; Dal Santo, V. Effect of Nature and Location of Defects on Bandgap Narrowing in Black TiO_2 Nanoparticles. *J. Am. Chem. Soc.* **2012**, *134*, 7600−7603.

(44) Chen, J.; Ding, Z.; Wang, C.; Hou, H.; Zhang, Y.; Wang, C.; Zou, G.; Ji, X. Black Anatase Titania with Ultrafast Sodium-Storage Performances Stimulated by Oxygen Vacancies. *ACS Appl. Mater. Interfaces* **2016**, *8*, 9142−9151.

(45) Lei, F.; Sun, Y.; Liu, K.; Gao, S.; Liang, L.; Pan, B.; Xie, Y. Oxygen Vacancies Confined in Ultrathin Indium Oxide Porous Sheets for Promoted Visible-Light Water Splitting. *J. Am. Chem. Soc.* **2014**, *136*, 6826−6829.

(46) Wendt, S.; Sprunger, P. T.; Lira, E.; Madsen, G. K. H.; Li, Z.; Hansen, J. O.; Matthiesen, J.; Blekinge-Rasmussen, A.; Laegsgaard, E.; Hammer, B.; Besenbacher, F. The Role of Interstitial Sites in the Ti3d Defect State in the Band Gap of Titania. *Science* **2008**, *320*, 1755−1759.

(47) Zhang, N.; Jalil, A.; Wu, D.; Chen, S.; Liu, Y.; Gao, C.; Ye, W.; Qi, Z.; Ju, H.; Wang, C.; Wu, X.; Song, L.; Zhu, J.; Xiong, Y. Refining Defect States in $W_{18}O_{49}$ by Mo Doping: A Strategy for Tuning N_2 Activation towards Solar-Driven Nitrogen Fixation. *J. Am. Chem. Soc.* **2018**, *140*, 9434−9443.

(48) Li, H.; Shang, J.; Ai, Z.; Zhang, L. Efficient Visible Light Nitrogen Fixation with BiOBr Nanosheets of Oxygen Vacancies on the Exposed {001} Facets. *J. Am. Chem. Soc.* **2015**, *137*, 6393−6399.

(49) Li, H.; Shang, J.; Shi, J.; Zhao, K.; Zhang, L. Facet-Dependent Solar Ammonia Synthesis of BiOCl Nanosheets via a Proton-Assisted Electron Transfer Pathway. *Nanoscale* **2016**, *8*, 1986−1993.

(50) Wang, S.; Hai, X.; Ding, X.; Chang, K.; Xiang, Y.; Meng, X.; Yang, Z.; Chen, H.; Ye, J. Light-Switchable Oxygen Vacancies in Ultrafine Bi_5O_7Br Nanotubes for Boosting Solar-Driven Nitrogen Fixation in Pure Water. *Adv. Mater.* **2017**, *29*, 1701774.

(51) Zhao, Y.; Zhao, Y.; Waterhouse, G. I. N.; Zheng, L.; Cao, X.; Teng, F.; Wu, L.-Z.; Tung, C.-H.; O'Hare, D.; Zhang, T. Layered-Double-Hydroxide Nanosheets as Efficient Visible-Light-Driven Photocatalysts for Dinitrogen Fixation. *Adv. Mater.* **2017**, *29*, 1703828.

(52) Xie, X.-Y.; Xiao, P.; Fang, W.-H.; Cui, G.; Thiel, W. Probing Photocatalytic Nitrogen Reduction to Ammonia with Water on the Rutile TiO_2 (110) Surface by First-Principles Calculations. *ACS Catal.* **2019**, *9*, 9178−9187.

https://dx.doi.org/10.1021/acsami.0c17947
ACS Appl. Mater. Interfaces 2021, 13, 4975−4983